University of Nebraska - Lincoln

DigitalCommons@University of Nebraska - Lincoln

Faculty Publications, Department of Physics and Astronomy

Research Papers in Physics and Astronomy

6-14-2022

A Room-Temperature Ferroelectric Resonant Tunneling Diode

Zhijun Ma,

Qi Zhang

Lingling Tao

Yihao Wang

Daniel Sando

See next page for additional authors

Follow this and additional works at: https://digitalcommons.unl.edu/physicsfacpub

Part of the Physics Commons

This Article is brought to you for free and open access by the Research Papers in Physics and Astronomy at DigitalCommons@University of Nebraska - Lincoln. It has been accepted for inclusion in Faculty Publications, Department of Physics and Astronomy by an authorized administrator of DigitalCommons@University of Nebraska - Lincoln.

Authors

Zhijun Ma,; Qi Zhang; Lingling Tao; Yihao Wang; Daniel Sando; Jinling Zhou; Yizhong Guo; Michael Lord; Peng Zhou; Yongqi Ruan; Zhiwei Wang; Alex Hamilton; Alexei Gruverman; Evgeny Y. Tsymbal; Tianjin Zhang; and Nagarajan Valanoor

ADVANCED MATERIALS
www.advmat.de

A Room-Temperature Ferroelectric Resonant Tunneling Diode

Zhijun Ma, Qi Zhang, Lingling Tao, Yihao Wang, Daniel Sando, Jinling Zhou, Yizhong Guo, Michael Lord, Peng Zhou, Yongqi Ruan, Zhiwei Wang, Alex Hamilton, Alexei Gruverman, Evgeny Y. Tsymbal, Tianjin Zhang, and Nagarajan Valanoor**

Resonant tunneling is a quantum-mechanical effect in which electron transport is controlled by the discrete energy levels within a quantum-well (QW) structure. A ferroelectric resonant tunneling diode (RTD) exploits the switchable electric polarization state of the QW barrier to tune the device resistance. Here, the discovery of robust room-temperature ferroelectric-modulated resonant tunneling and negative differential resistance (NDR) behaviors in all-perovskite-oxide $BaTiO_3/SrRuO_3/BaTiO_3$ QW structures is reported. The resonant current amplitude and voltage are tunable by the switchable polarization of the $BaTiO_3$ ferroelectric with the NDR ratio modulated by ≈3 orders of magnitude and an OFF/ON resistance ratio exceeding a factor of 2×10^4. The observed NDR effect is explained an energy bandgap between Ru-t_{2g} and Ru-e_g orbitals driven by electron–electron correlations, as follows from density functional theory calculations. This study paves the way for ferroelectric-based quantum-tunneling devices in future oxide electronics.

1. Introduction

A potential well sandwiched between two potential barriers is called a quantum-well (QW) structure. An increased probability of electron tunneling occurs when the electron injection energy aligns with a discrete energy level within the well. This phenomenon, known as resonant tunneling, is exploited in resonant tunneling diodes (RTDs).[1]

Since the first observation of resonant tunneling in double-barrier structures by Chang et al.,[2] RTDs have attracted significant attention as functional high-speed devices and circuits for applications in radio-frequency communications and spintronics.[3–5] Resonant tunneling is often accompanied by negative differential resistance (NDR), which represents a decrease in the electric current resulting from the alignment and subsequent misalignment of the injection and QW energy levels under increasing bias. It could be argued that resonant tunneling and NDR effects are among the most fascinating features of RTDs, from the perspective of both fundamental physics and nanoelectronic device applications.[6–8]

To date, room-temperature resonant tunneling and accompanying NDR have predominantly been studied in Si-based or III–V compound semiconductors.[5,8] As the demand for faster and more compact electronic devices pushes these conventional technologies toward their physical limits, novel material platforms such as complex oxides and 2D materials are now gaining significant attention.[9,10]

Complex oxide materials have long been known to possess a rich variety of physical properties such as ferroelectricity, colossal magnetoresistance, multiferroicity, a quantum Hall effect, and superconductivity.[11–13] The rapid advances in the development of layer-by-layer oxide heteroepitaxy of the past several decades has enabled fabrication of atomically perfect

Z. Ma, Y. Wang, P. Zhou, Y. Ruan, Z. Wang, T. Zhang
Ministry of Education Key Laboratory for the Synthesis and Application of Organic Functional Molecules
Ministry of Education Key Laboratory for the Green Preparation and Application of Functional Materials
Hubei University
Wuhan 430062, P. R. China
E-mail: zhangtj@hubu.edu.cn

Z. Ma, Q. Zhang, D. Sando, J. Zhou, M. Lord, N. Valanoor
School of Materials Science and Engineering
University of New South Wales
Sydney 2052, Australia

The ORCID identification number(s) for the author(s) of this article can be found under https://doi.org/10.1002/adma.202205359.

© 2022 The Authors. Advanced Materials published by Wiley-VCH GmbH. This is an open access article under the terms of the Creative Commons Attribution License, which permits use, distribution and reproduction in any medium, provided the original work is properly cited.

DOI: 10.1002/adma.202205359

Q. Zhang, D. Sando, J. Zhou, M. Lord, A. Hamilton, N. Valanoor
The Australian Research Council Centre for Excellence in Future Low Energy Electronics Technologies
UNSW
Sydney 2052, Australia
E-mail: nagarajan@unsw.edu.au

L. Tao, A. Gruverman, E. Y. Tsymbal
Department of Physics and Astronomy and Nebraska Center for Materials and Nanoscience
University of Nebraska
Lincoln, NE 68588, USA

Y. Guo
Institute of Microstructure and Properties of Advanced Materials
Beijing University of Technology
Beijing 100124, P. R. China

A. Hamilton
School of Physics
University of New South Wales
Sydney 2052, Australia

 © 2022 The Authors. Advanced Materials published by Wiley-VCH GmbH

all-oxide heterostructures with ultrathin tunneling barriers.[14] Despite these developments, investigation of the resonant tunneling behavior in complex oxide-based QW structures is still at a nascent stage. Recently, NDR was experimentally realized at cryogenic temperatures in a QW superlattice designed by inserting atomically thin $LaTiO_3$ (LTO) between $SrTiO_3$ (STO) barrier layers.[15] In another study, strong quantum oscillations of electrical conductance were observed in $La_{0.7}Sr_{0.3}MnO_3$ (LSMO)/$BaTiO_3$ (BTO)/LSMO multiferroic tunnel junctions (MFTJs) below 100 K[16] and attributed to charged domain wall-assisted resonant tunneling.[17] These results point to the promising functional properties of RTDs based on complex oxides.

Simultaneously, the various demonstrations of robust ferroelectricity down to a few unit cells at room temperature[18] in the past decade triggered the quantum era of ferroelectrics. The perspective by Tsymbal and Kohlstedt[19] ushered in the era of the ferroelectric tunnel junctions (FTJs)[14,20–22] and related tunneling electro-resistance (TER) effects.[23–26] Furthermore, various emergent properties have been combined in complex oxide-based tunnel junctions to result in multifunctional devices. For example, MFTJs with a ferroelectric barrier sandwiched between two ferromagnetic electrodes can provide the combined functionalities of magnetic tunnel junctions (MTJs) and FTJs, useful in multilevel memories and electric-field-controlled spintronics.[27,28]

These advances bring us to a unique crossroads—can we exploit the intriguing interplay between electron tunneling and ferroelectric polarization[29–31] to modulate resonant tunneling at room temperature? That is, if ferroelectricity is combined with the QW structure, can the ferroelectric polarization switchable by an applied electric field control the QW energy levels? This would bring an unprecedented set of advantages, including a robust signal-to-noise ratio at room temperature, and the possibility (in the case of a multiferroic barrier) to use external magnetic fields to modulate the resonant tunneling behavior.[16] Previous work by Wu et al. has demonstrated ferroelectric modulation of resonant tunneling in $LaAlO_3$ (LAO)/BTO/LAO structures. Their design used the ferroelectric BTO as the QW, which has a bandgap of similar order as the barrier.[32] In contrast, the use of a metallic (i.e., lacking a distinct bandgap[33]) perovskite oxide such as $SrRuO_3$ (SRO) as the QW, one could expect a significantly enhanced modulation effect of resonant tunneling.

Here, we demonstrate room-temperature polarization-controlled resonant tunneling and NDR in all-perovskite-oxide BTO/SRO/BTO heterostructures. Our density functional theory (DFT) calculations show that the observed NDR behavior can be explained by a bandgap between excited Ru-t_{2g} and Ru-e_g states induced by electron–electron correlations. The NDR displays three key characteristics that can be exploited in electronic devices. First, once the ferroelectric polarization is "SET" with a fixed voltage, the resonant voltage scales directly with the magnitude of a "WRITE" voltage. The current ratio can then be modulated by up to 3 orders of magnitude depending on the chosen "SET" and "WRITE" voltage bias combinations. Second, the magnitude of the peak current can be controlled by the "SET" direction of polarization. Finally, we show that the NDR behavior is maintained for thicker SRO well widths (up to 4.5 nm) and that a large OFF/ON ratio over 20 000 can be obtained.

2. Results and Discussion

Epitaxial BTO/SRO/BTO heterostructures were grown by pulsed laser deposition onto (001) Nb-doped STO (NSTO) substrates (see Experimental Sections). The RTD devices are completed by the growth of Pt top electrodes (100 µm in diameter). The film configuration and atomic structure of the BTO/SRO/BTO RTDs are sketched in **Figure 1**a. The thickness of each BTO layer is 3.5 nm, while the thickness of SRO is varied from 1.5 to 4.5 nm. X-ray diffraction (XRD) characterization confirms single orientation, epitaxial films with no parasitic phases (Figures S1 and S2, Supporting Information). Figure 1b presents a cross-sectional scanning transmission electron microscopy (STEM) image of a representative BTO (3.5 nm)/SRO (3 nm)/BTO (3.5 nm) heterostructure. Clean interfaces are observed, suggesting good film quality and homogeneous layer thicknesses. Using the NSTO substrate as reference (a_{NSTO} = 3.905 Å), the lattice parameters of BTO and SRO were extracted (**Table 1**). Both the bottom (with in-plane lattice parameter a_{BTO_1} = 3.90 Å) and top (a_{BTO_2} = 3.95 Å) BTO layers are subject to significant in-plane compressive strain (compared to bulk BTO with a_{BTO_bulk} = 3.99 Å; ref. [34]). As a consequence, the out-of-plane lattice parameter is elongated, with bottom c_{BTO_1} = 4.19 Å and top c_{BTO_2} = 4.06 Å, respectively. Regarding the SRO layer, we find that it grows with an orthorhombic structure in the $(110)_o$ orientation. The lattice spacings are found to be a_{SRO} = 5.53 Å and b_{SRO} = 5.57 Å, consistent with the reported epitaxially constrained lattice parameters of SRO thin films in the *Pbnm* space group[35] (measurement details in Figure S3, Supporting Information). The importance of this orthorhombic SRO in the QW structure is discussed in **Figure 2**.

Scanning probe microscopy was used to inspect the surface quality and ferroelectric switching. Atomic force microscopy (AFM) topography images of BTO/SRO (3 nm)/BTO film reveal that the heterostructure has smooth surfaces (root mean square roughness of 350 pm) without pinholes or large particles (Figure S4a, Supporting Information). The butterfly-shaped switching spectroscopy piezoresponse force microscopy (SS-PFM) amplitude and square phase hysteresis loops (Figure S4b, Supporting Information) demonstrate robust ferroelectric switching. Moreover, piezoresponse force microscopy (PFM) phase and amplitude images of box-in-box poling domain patterns in Figure S4c,d (Supporting Information) further confirm the ferroelectric nature of the QW structure.

Having confirmed that the QW heterostructures are fabricated with atomically sharp interfaces and demonstrate robust ferroelectricity, we now discuss the transport characteristics. The pulse train used for the current–voltage (I–V) measurements is shown in Figure 1c. Figure 1d presents the obtained I–V response for a BTO/SRO/BTO RTD for the voltage pulse range between ±4 V for a 1.5 nm-thick SRO well. Reproducible NDR behavior is observed for the positive bias direction. The absence of a peak in the negative bias direction may be attributed to the large current level which hinders the observation of an NDR effect.[15]

The smooth NDR peaks in our I–V curves are in contrast with the abrupt shaped curves reported for various complex oxide junction structures.[36–38] Given the present QW design structure, a smooth NDR peak is expected to be the hallmark

© 2022 The Authors. Advanced Materials published by Wiley-VCH GmbH

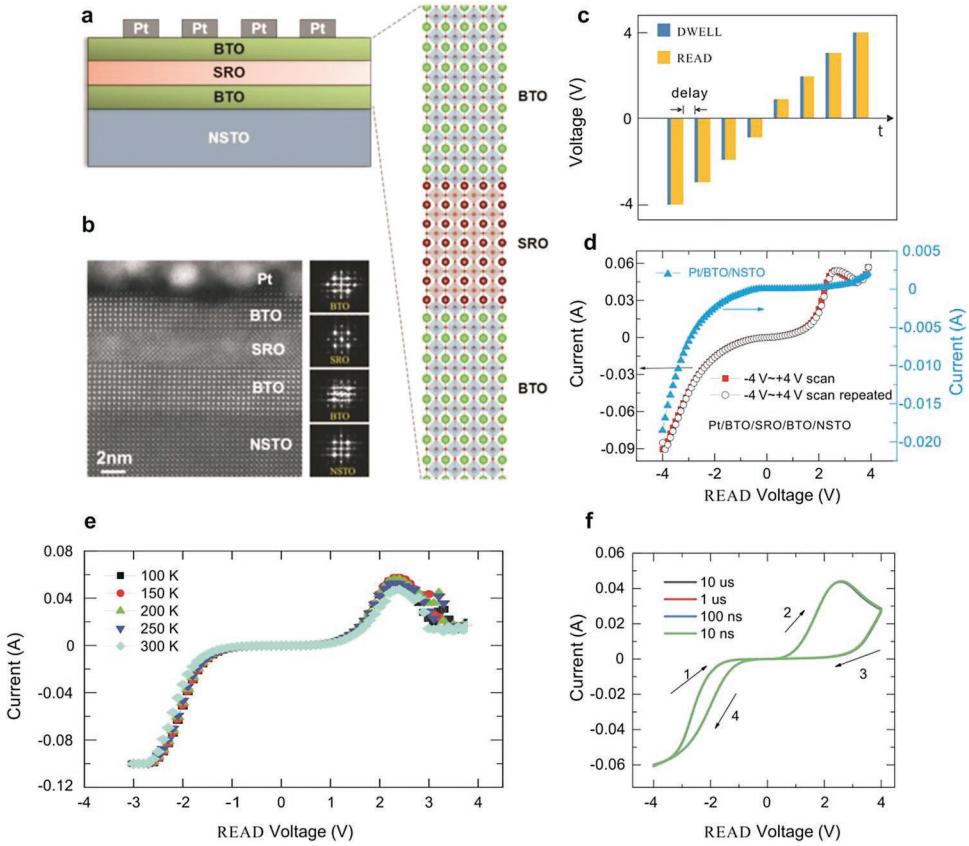

Figure 1. Device structure and NDR behavior of BTO/SRO/BTO RTDs. a) Schematic of the BTO/SRO/BTO RTD configuration. b) Cross-sectional STEM of a BTO (3.5 nm)/SRO (3 nm)/BTO (3.5 nm) RTD and fast Fourier transform (FFT) patterns of each layer. The image is observed along the NSTO [010] zone axis. c) Pulse profile for *I–V* measurements. d) *I–V* curves of Pt/BTO (3.5 nm)/SRO (1.5 nm)/BTO (3.5 nm)/NSTO RTD and Pt/BTO (3.5 nm)/NSTO heterostructure. e) Temperature-dependent and f) pulse-width-dependent *I–V* characteristics of BTO (3.5 nm)/SRO (1.5 nm)/BTO (3.5 nm) RTDs. The arrows indicate the direction of the voltage sweep.

of resonant tunneling.[15] Confirmation of this hypothesis was obtained by measuring *I–V* curves on a reference Pt/BTO (3.5 nm)/NSTO single-barrier junction. As shown in the blue data points in Figure 1d, in this reference sample the current exhibits a rectification effect, showing no evidence of NDR.

Figure 1e shows temperature dependence *I–V* of the same device which reveals a resonant tunneling feature for all temperatures. On the whole, the resonant tunneling peak current level increases as temperature decreases, which is more obvious in the negative voltage region (detail in Figure S5, Supporting Information). Such temperature-dependent increase of the current can be ascribed to the enhanced carrier mobility at low temperatures. In addition, to rule out the possibility that the NDR effect might be an interface trapping effect, fast pulses without delay have been used to study the frequency dependent *I–V* behavior of an RTD. The step of the applied voltage is reduced to 20 from 100 mV used in previous measurements. As shown in Figure 1f, the NDR effect can be clearly observed with the pulse width reduced to 10 ns. Most notably, the curves are nearly independent of the pulse width. Therefore, we can furthur confirm that the NDR effect origins from the RT effect.

Table 1. Lattice parameters of the BTO (3.5 nm)/SRO (3 nm)/BTO (3.5 nm) heterostructure.

Materials	*a* (Å)	*c* or *b* (Å)
Top BTO layer (pseudocubic)	3.95 ± 0.02	4.06 ± 0.03 (*c*)
Bottom BTO layer (pseudocubic)	3.90 ±0.02	4.19 ± 0.02 (*c*)
NSTO substrate	3.905	3.905 (*c*)
SRO layer (pseudocubic)	3.91 ± 0.02	3.94 ± 0.04 (*c*)
SRO layer (orthorhombic, *Pbnm*)	5.53 ± 0.04	5.57 ± 0.05 (*b*)

For practical RTD devices, a small tunnel lifetime (τ) of electrons on the resonant states helps to speed up the transport and relaxation processes.[39] The tunnel lifetime τ, defined as $\tau = \hbar/2\Delta E$, where $\hbar$ is the reduced Planck's constant and ΔE the half width at half maximum of the resonant peak, is found to be an average value of 0.47 fs for the BTO/SRO/BTO RTD shown in Figure 1d. This value is orders of magnitude smaller than that obtained in semiconductor QWs[40] and superior to the lifetime (≈0.7 fs) obtained in a quantum oxide superlattice.[15]

To explain the origins of the NDR behavior, we performed DFT calculations (see Experimental Sections), specifically considering the band structure and band alignment within the SRO QW. Bulk SRO crystallizes in an orthorhombic structure in the *Pbnm* space group.[41] (Figure 2a). Figure 2b shows the orbital-projected density of states (PDOS) of bulk SRO from generalized gradient correction (GGA)[42] plus

© 2022 The Authors. Advanced Materials published by Wiley-VCH GmbH

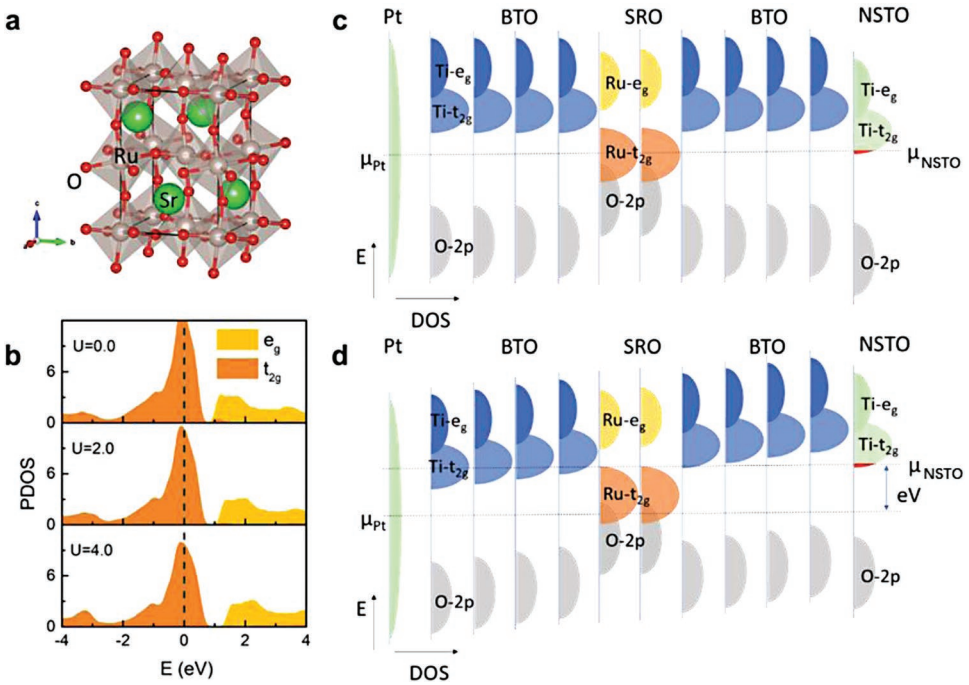

Figure 2. Results of density functional theory calculations. a) Atomic structure of orthorhombic SRO (space group *Pbnm*). b) Projected density of states (PDOS) onto Ru-t_{2g} and Ru-e_g orbitals for different Hubbard-*U* corrections. The vertical dashed line denotes the position of the Fermi energy. c,d) Schematic band alignment for the Pt/BTO/SRO/BTO/NSTO QW structure under zero bias (c) and finite bias (d).

Hubbard-*U* correction on the Ru-4d orbital, reflecting the effect of the on-site electron–electron Coulomb repulsion. Consistent with previous results,[43] we find that the Ru-t_{2g} bands dominate around the Fermi energy while the Ru-e_g bands lie above the Fermi energy. The Hubbard-*U* correction pushes the Ru-e_g bands up in energy, while the Ru-t_{2g} bands become more localized. This leads to the opening of a bandgap between the Ru-t_{2g} and Ru-e_g states above the Fermi energy due to electron–electron correlations.

The presence of the bandgap in the spectrum of excited states of SRO plays a key role in the observed NDR effect. Figure 2c shows the schematic band alignment in the QW structure. With small applied bias voltage, electron tunneling between the NSTO and Pt electrodes occurs through the confined Ru-t_{2g} states in the bandgap of BTO. When the applied (positive) bias increases, the narrowly populated NSTO band moves up in energy scanning through the Ru-t_{2g} states eventually reaching the top of the Ru-t_{2g} band. At this bias, the shallow NSTO band enters the bandgap between Ru-t_{2g} and Ru-e_g states (Figure 2d), and the SRO layer acts as an additional barrier, resulting in the current drop and hence the NDR effect. We thus conclude that the bandgap between Ru-t_{2g} and Ru-e_g states driven by electron–electron correlations is responsible for the observed NDR effect in this Pt/BTO/SRO/BTO/NSTO QW structure.

Having explained the origin of the NDR effect in our RTDs, we next demonstrate modulation of the resonant tunneling behavior of the QW structures as a function of up and down "SET" ferroelectric polarization directions. The corresponding pulse profiles for each "SET" direction are illustrated in **Figure 3**a,b.

For both cases, a smooth NDR peak is observed (Figure 3c,d), implying that RT occurs for both polarization directions. This observation is repeatable on multiple devices (statistics given in Figure S6, Supporting Information), and the RTDs exhibit good retention and fatigue performance (Figure S7, Supporting Information). Following a fixed positive "SET" pulse (+6 V), the resonant peaks show two pronounced effects (Figure 3c) with increasing "WRITE" voltage. Both the peak current magnitude and the resonance voltage systematically increase when the "WRITE" voltage is changed progressively from −3.5 V to −5 V. Note that no resonant peak is observed for smaller pulse height of −2 to −3 V. In contrast, using a negative "SET" voltage pulse of −6 V yields the opposite behavior (Figure 3d). Here, the first resonance peak is observed at +2 V "WRITE" voltage and the peak shifts to higher values, eventually vanishing. This behavior is summarized in Figure 3e, where the peak current and voltages are plotted as a function of "WRITE" voltage, demonstrating unequivocal ferroelectric tuning of the RT. We find that the resonance peak current magnitude and voltage are tunable (by a factor of 3 and 1.5, respectively) by changing both magnitude and direction of the polarization.

These trends in the polarization-modulated *I*–*V* characteristics can be fully captured in a single current ratio plot (Figure 3f). Here, the current ratios for "WRITE" voltages of the same magnitude but opposite polarity are presented as a function of increasing positive "READ" bias. The shape of each pair of the current ratio plots is a direct reflection of how the current transport occurs for each individual "WRITE" magnitude.

For instance, no resonance peak is observed at negative −2 V "WRITE" voltage (Figure 3c), whilst at +2 V "WRITE" voltage, the peak appears at +2.5 V "READ" bias (Figure 3d). Hence for small "WRITE" voltage magnitudes (i.e., 2 V), the current ratio is the highest. The current ratio decreases smoothly,

© 2022 The Authors. Advanced Materials published by Wiley-VCH GmbH

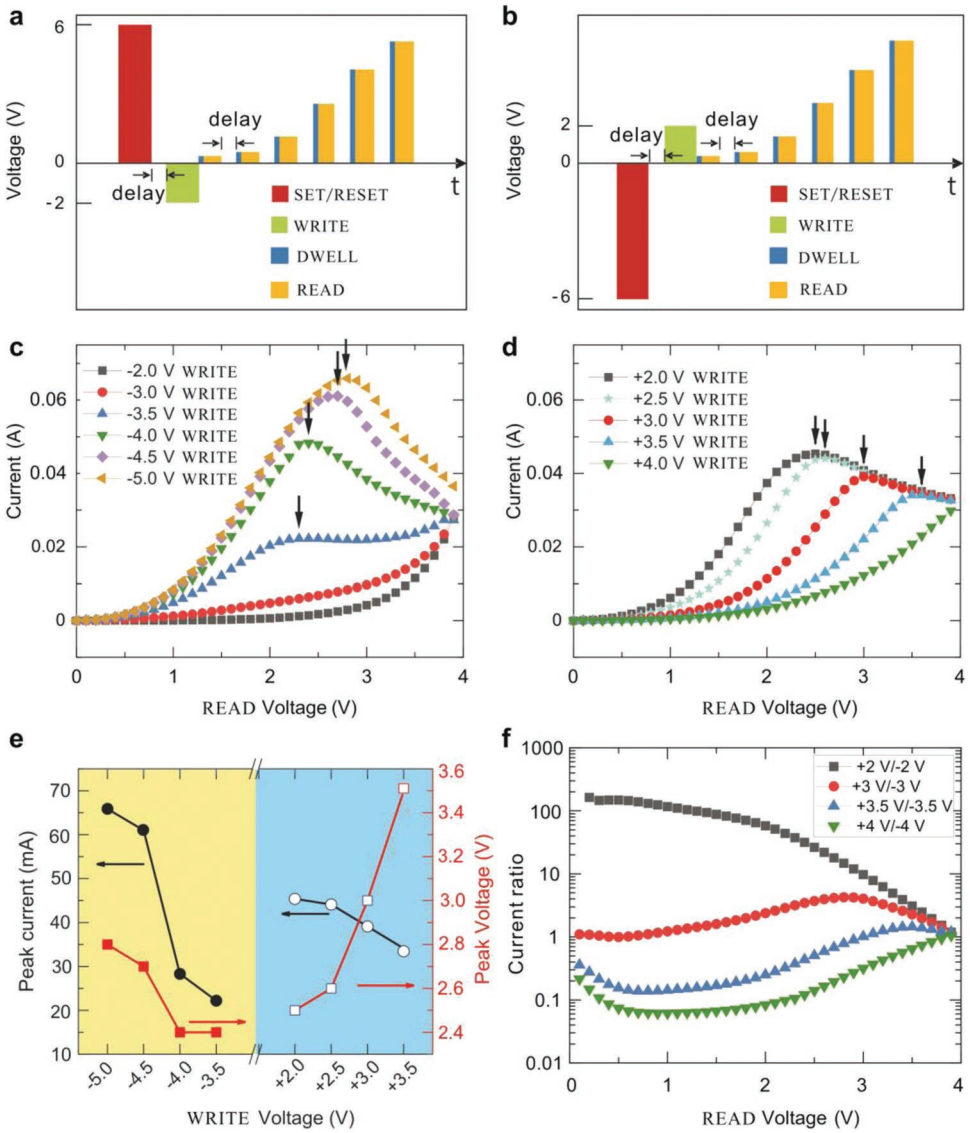

Figure 3. Ferroelectric polarization modulated RT behavior of a BTO (3.5 nm)/SRO (1.5 nm)/BTO (3.5 nm) RTD. a,b) Pulse profiles for *I–V* measurements with positive and negative "SET" bias, respectively. c,d) *I–V* curves for different "WRITE" pulse amplitudes corresponding to (a) and (b), respectively. In (c), BTO films were "SET" by a +6 V pulse followed by a negative "WRITE" voltage pulse (–2 to –5 V) before each measurement. In (d), BTO films were "SET" by a –6 V pulse followed by a positive "WRITE" voltage pulse (+2 to +4 V) before each measurement. The arrows in (c) and (d) indicate the peak current. e) Peak current (circle) and peak voltage (square) as a function of "WRITE" voltage. The filled data points correspond to positive "SET" voltage and negative "WRITE" voltage, and vice versa for the open data points. f) Current ratio between different polarization state caused by first two pulses in (c) and (d). In the legend, the positive and negative voltages correspond to the "WRITE" voltage in (d) and (c), respectively.

eventually converging to a value of 1, with increasing bias. This is attributed to two counter effects: first, for the positive "WRITE" pulse, the current decreases following the resonant tunneling peak, and second, for the negative "WRITE" pulse, the current magnitude steadily increases.

For higher values of "WRITE" voltage (e.g., +3 V/–3 V), the shape of the current ratio curve dramatically changes. For the positive "WRITE" voltage, a clear peak in the current profile is observed at +3.0 V "READ" bias (Figure 3d), while for the negative "WRITE" voltage, there is just a smooth increase (Figure 3c). As a result, the corresponding current ratio plot in Figure 3f mirrors this rise and fall, with the peak being less pronounced.

On the other hand, the current ratios for the highest "WRITE" voltages show an almost reverse trend. This is attributed to the fact that the resonance peak appears for the negative "WRITE" voltages and is subdued or non-existent for positive "WRITE" voltages. Taken together, this explains the lenticular shape of the current ratios in Figure 3f, which unequivocally demonstrates the NDR ratio within the same junction can be modulated over nearly three orders of magnitude simply by varying the "SET" and "WRITE" voltages.

The microscopic origins of the observed NDR phenomena in terms of nanoscale domain structures and associated conductivity changes within the ferroelectric have been studied using a combination of PFM/conductive AFM (CAFM) scans.

© 2022 The Authors. Advanced Materials published by Wiley-VCH GmbH

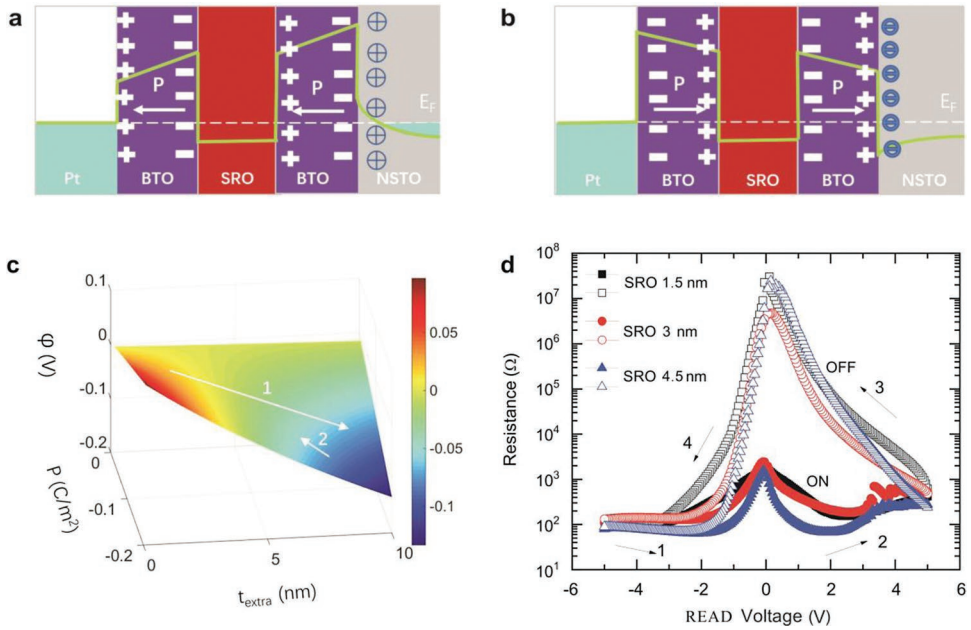

Figure 4. Charge distribution and energy-band diagrams at zero bias and potential well width modulated RT behavior and resistance. a,b) Charge distribution and energy-band diagrams for ferroelectric polarization pointing to Pt top electrode and to bottom NSTO, respectively. The "plus" and "minus" symbols represent positive and negative bound charges, respectively. The "circled plus" and "circled minus" symbols in NSTO represent ionized donors and electrons, respectively. E_F denotes the Fermi level. c) Calculated BTO polarization and extra barrier-thickness-dependent potential of SRO in Pt/BTO (3.5 nm)/SRO (1.5 nm)/BTO (3.5 nm)/NSTO RTD. Negative values of *P* correspond to the case where the ferroelectric polarization points toward the top Pt electrode. d) *R*–*V* curves for different SRO thicknesses and resistance states. The arrows indicate the direction of the voltage sweep.

The domain orientation and portion as a function of applied electric field magnitude (corresponding to the "SET" and "WRITE" bias) and scanning times are investigated (data are shown in Figures S8 and S9, Supporting Information), demonstrating the domain switching dynamics. CAFM data (in Figure S10, Supporting Information) reveals a higher conductivity in downward domain regions, which is consistent with the data in Figure 3.

To explain the observed behavior analytically, we consider the NSTO bottom electrode as an n-type semiconductor with electrons being the majority carriers. As shown in **Figure 4**a, the negative polarization charges at the BTO/NSTO interface repel electrons when the ferroelectric polarization points upward (i.e., to Pt), developing a depletion region, effectively increasing the barrier thickness. The coercive voltage required to switch the polarization upward and downward are +2 V and −4 V, respectively (Figure S11, Supporting Information). As the "WRITE" positive pulse is increased from +2 V to +4 V (Figure 3d), the ferroelectric polarization switches back to the upward direction, and more negative ferroelectric bound charges accumulate at the BTO/NSTO interface, thus widening the effective barrier width. To interpret the behavior shown in Figure 3d, both the effective polarization strengths and extra barrier width should be considered. One simple way is to investigate the variation of the potential in SRO well.

Figure 4c shows the calculated potential in the SRO well (φ) as a function of the effective upward ferroelectric polarization magnitude (P) and additional barrier thickness caused by the depletion region at the NSTO/BTO interface (t_{extra}) at zero bias voltage (see the Analytical Calculations Section in the Experimental Section). We find that as the effective upward polarization and extra barrier width increase, the potential of the SRO well drops (as indicated by arrow 1 in Figure 4c), which then raises the quantized energy levels. This pushes the resonant peak to the right as the "WRITE" voltage is increased, which is indeed observed upon increase of the "WRITE" pulse from +2 to +4 V (Figure 3d). This also could explain why we are not able to observe resonant peaks for −2 V and −3 V pulses in Figure 3c; it is a combined effect of the relatively large effective up polarization and resultant extra barrier width, which triggers the relatively low potential of SRO (see arrow 2 in Figure 4c).

Second, we consider a larger "WRITE" pulse height (i.e., <−4 V) in Figure 3c, which is sufficient to switch the ferroelectricity polarization down. In this case, in contrast to the positive "SET" voltage case, negative and positive polarization charges accumulate at the bottom SRO/BTO and BTO/NSTO interfaces, respectively (Figure 4b). The former decreases the potential of the SRO well and raises the quantized energy levels; accordingly, the latter leads to the attraction of electrons in NSTO to accumulate at the interface and so the energy band bends down at the interface and no extra barrier forms. The effect is strengthened as the "WRITE" pulse height is increased. As a result, the resonant peak once again shifts toward the right with increasing "WRITE" pulse height in Figure 3c.

We next investigated how the well width influences device resistance switching behavior. This is summarized in Figure 4d where we plot changes in the junction resistance with the full bias cycle (resistance–voltage *R*–*V* curves) for three different SRO layer thicknesses (1.5, 3, and 4.5 nm). The single-sweep *I*–*V* data are given in Figure S12 (Supporting Information). A dominant NDR behavior is observed for all SRO thicknesses, with a large OFF/ON ratio obtained for

© 2022 The Authors. Advanced Materials published by Wiley-VCH GmbH

the larger well-widths; for instance, at a "READ" voltage of +0.1 V, the OFF/ON ratios reach as high as 2.3×10^4 (SRO 4.5 nm). The *R*–*V* curves for different SRO well widths in Figure 4d reveal a strongly hysteretic behavior, similar to previous reports on quantum oxide superlattices.[15] Importantly, the enhanced OFF/ON ratio, in conjunction with the dip of the *R*–*V* curve for the ON state near the resonant peak (Figure 4d), further confirm RT in these devices. The retention and cyclic endurance of a RTD device are shown in Figure S13 (Supporting Information). This indicates that we do not necessarily need an ultrathin well to achieve RT in this system, which: i) removes a significant thin-film fabrication constraint and ii) promises more robust device performance.

3. Conclusions

We have reported smooth and robust room temperature NDR behavior in Pt/BTO/SRO/BTO/NSTO QW heterostructures, resulting from resonant tunneling. The ferroelectric polarization direction is exploited to tune the resonant tunneling behavior and achieve one of the largest OFF/ON ratios ever reported for quantum devices with BTO as a ferroelectric barrier layer. Our study opens the door to room temperature ferroelectric-based resonant tunneling diodes for use in future oxide nanoelectronics.

4. Experimental Section

Sample Fabrication: $BaTiO_3$ (BTO)/$SrRuO_3$ (SRO)/BTO trilayers were grown on (001)-oriented 0.7 wt% Nb-doped STO (NSTO) substrates by pulsed laser deposition (PLD) (KrF excimer laser, λ = 248 nm) at a deposition temperature of 700 °C. BTO films were deposited at 1 Hz repetition, under oxygen atmosphere of 10 Pa. The corresponding parameters for depositing SRO were 2 Hz and 14 Pa. The thickness of SRO was varied by controlling the number of pulses used during growth. After deposition, the samples were kept at 700 °C for 10 min and subsequently cooled to room temperature in an oxygen pressure of 10 Pa. Top Pt electrodes of 100 µm in diameter were patterned at room temperature by DC sputtering through a shadow mask, under 0.5 Pa of pure argon pressure and power of 40 W. Cross-section STEM samples were prepared by focused ion-beam (FIB) techniques carried out on FEI Scios Dual Beam.

Structural and Scanning Probe Microscopy Characterization: The atomic structure of the BTO/SRO/BTO trilayers on NSTO was inspected using high-angle annular dark-field scanning transmission electron microscopy (HAADF-STEM) on aberration-corrected FEI Titan Themis electron microscope operated at 300 kV. Surface topography of the top BTO thin film was tested using a commercial atomic force microscope system (Cypher S, Asylum Research, US). The structure and orientation of BTO films was also characterized by X-ray diffraction (XRD) using Cu $K_{\alpha 1}$ radiation (λ = 1.5406 Å, Bruker D8 Discover) (Figures S1 and S2, Supporting Information). High-angle θ–2θ scans were used to confirm the orientation while φ-scans and asymmetric reciprocal space maps were used to confirm epitaxial growth of BTO.

Electrical Measurements: Ferroelectric domain structures and domain switching behavior of the BTO/SRO/BTO trilayers were studied using the piezoresponse force microscopy (PFM) (Cypher S, Asylum Research, US) with Pt/Cr coated conductive probes (ElectriMulti 75G, BudgetSensors, Bulgaria). The measurements were conducted under the Dual AC Resonance Tracking (DART) mode. A Keithley 2400 SourceMeter was used to measure current–voltage (*I*–*V*) characteristics of the RTDs. Each pulse duration was composed of a "DWELL" time of 1 ms and reading (measuring) time of 20 ms. The gap between two pulses (delay time) was 1 s.

The data in Figure 3 were collected using the following protocol. For all measurements the "SET" voltage pulse was +6 or −6 V. In Figure 3a, the first pulse of +6 V is a "SET" voltage for the first *I*–*V* measurement or a "RESET" voltage for the subsequent measurements. It is followed by a "WRITE" voltage in the range between −2 V and −5 V. Both pulses are 1s in width. Other parameters are the same with those in Figure 1c. A similar procedure was used for the opposite polarization state on the same pad with a "SET/RESET" pulse of −6 V followed by a "WRITE" voltage between +2 and +4 V (Figure 3b). In both cases, the "READ" voltage sweeps were the same. The pulse profile for Figure 4d is the same as that in Figure 1c except for the scan range (from −5 V to +5 V) and rate (0.05 V s^{-1}). Resistance values reported here were obtained by the ratio of applied voltage to the current ($R = V/I$). For both PFM and *I*–*V* measurements, the external bias was applied to the bottom electrode NSTO. Measurements in Figure 1f were performed using a Keithley 4200 SourceMeter to apply fast pulses. All measurements (except Figure 1e) were conducted at room temperature.

Density Functional Theory (DFT) Calculations: DFT calculations were performed using the plane-wave ultrasoft pseudopotential method[44] implemented in Quantum ESPRESSO.[45] An energy cutoff of 680 eV and $10 \times 10 \times 8$ ($20 \times 20 \times 16$) *k*-point mesh were used for self-consistent projected density of states (PDOS) calculations. The lattice constants and atomic coordinates for bulk SRO were used in the calculations.[42]

Analytical Calculations: In the calculation of BTO polarization and extra barrier thickness-dependent potential of SRO (Figure 4c), the two ferroelectric films were assumed to be identical in thickness (t_f), and the SRO layer was treated as an ideal equipotential for simplicity. The potential of SRO (φ) could be obtained by using a Thomas–Fermi model on screening and imposing short-circuit boundary conditions[46] as

$$\varphi = \varphi_0 - \frac{t_f}{\varepsilon_f}(\sigma_s - P) \tag{1}$$

where

$$\varphi_0 = -\frac{\delta_{e1}}{\varepsilon_{e1}}\sigma_S \tag{2}$$

and

$$\sigma_S = \frac{\frac{2t_f}{\varepsilon_f}P}{\frac{t_{extra}}{\varepsilon_{extra}} + \frac{2t_f}{\varepsilon_f} + \frac{\delta_{e1}}{\varepsilon_{e1}} + \frac{\delta_{e2}}{\varepsilon_{e2}}} \tag{3}$$

σ_S is the screening charge per unit area in Pt. The screening length (δ_{e1}) and dielectric permittivity (ε_{e1}) of Pt were taken as 0.45 Å and $2\varepsilon_0$ (where ε_0 = vacuum dielectric constant), respectively.[47] For the NSTO electrode, the corresponding values are assumed to be 1 Å (δ_{e2}) and $10\varepsilon_0$ (ε_{e2}), respectively. The dielectric permittivity of BTO and extra barrier were taken as $90\varepsilon_0$ (ε_f) and $290\varepsilon_0$ (ε_{extra}), respectively.[46,48]

Supporting Information

Supporting Information is available from the Wiley Online Library or from the author.

Acknowledgements

Z.M. and Q.Z. contributed equally to this work. Z.M. and T.Z. acknowledge the support of the National Natural Science Foundation of China (Grant Nos. 11574073 and 11774083). Q.Z., D.S., A.H., and N.V. would like to acknowledge the support of Australian Research Council (ARC) Discovery Project and Australian Research Council Centre of Excellence in Future Low-Energy Electronics Technologies (Project No. CE170100039). E.Y.T. and L.T. acknowledge the support from the National

© 2022 The Authors. Advanced Materials published by Wiley-VCH GmbH

Science Foundation (NSF) through the MRSEC (NSF Award DMR-1420645) and EPSCoR RII Track-1 (NSF Award OIA-2044049) programs.

Open access publishing facilitated by University of New South Wales, as part of the Wiley - University of New South Wales agreement via the Council of Australian University Librarians.

Conflict of Interest

The authors declare no conflict of interest.

Data Availability Statement

The data that support the findings of this study are available from the corresponding author upon reasonable request.

Keywords

ferroelectrics, negative differential resistance, quantum-well structures, resonant tunneling diodes

Received: June 14, 2022
Published online:

[1] L. L. Chang, E. E. Mendez, C. Tejedor, *Resonant Tunneling in Semiconductors: Physics and Applications*, Plenum Press, New York **1991**.
[2] L. L. Chang, L. Esaki, R. Tsu, *Appl. Phys. Lett.* **1974**, *24*, 593.
[3] S. Yuasa, T. Nagahama, Y. Suzuki, *Science* **2002**, *297*, 234.
[4] A. Slobodskyy, C. Gould, T. Slobodskyy, C. R. Becker, G. Schmidt, L. W. Molenkamp, *Phys. Rev. Lett.* **2003**, *90*, 246601.
[5] M. Feiginov, H. Kanaya, S. Suzuki, M. Asada, *Appl. Phys. Lett.* **2014**, *104*, 243509.
[6] L. Britnell, R. V. Gorbachev, A. K. Geim, L. A. Ponomarenko, A. Mishchenko, M. T. Greenaway, T. M. Fromhold, K. S. Novoselov, L. Eaves, *Nat. Commun.* **2013**, *4*, 1794.
[7] L. N. Nguyen, Y. W. Lan, J. H. Chen, T. R. Chang, Y. L. Zhong, H. T. Jeng, L. J. Li, C. D. Chen, *Nano Lett.* **2014**, *14*, 2381.
[8] A. Ramesh, P. R. Berger, R. Loo, *Appl. Phys. Lett.* **2012**, *100*, 092104.
[9] S. Manipatruni, D. E. Nikonov, C. C. Lin, T. A. Gosavi, H. Liu, B. Prasad, Y. L. Huang, E. Bonturim, R. Ramesh, I. A. Young, *Nature* **2019**, *565*, 35.
[10] M. M. Waldrop, *Nature* **2016**, *530*, 144.
[11] Y. Tokura, H. Y. Hwang, *Nat. Mater.* **2008**, *7*, 694.
[12] R. Ramesh, D. G. Schlom, *MRS Bull.* **2011**, *33*, 1006.
[13] R. Ramesh, D. G. Schlom, *Nat. Rev. Mater.* **2019**, *4*, 257.
[14] A. Gruverman, D. Wu, H. Lu, Y. Wang, H. W. Jang, C. M. Folkman, M. Y. Zhuravlev, D. Felker, M. Rzchowski, C. B. Eom, E. Y. Tsymbal, *Nano Lett.* **2009**, *9*, 3539.
[15] W. S. Choi, S. A. Lee, J. H. You, S. Lee, H. N. Lee, *Nat. Commun.* **2015**, *6*, 7424.
[16] G. Sanchez-Santolino, J. Tornos, D. Hernandez-Martin, J. I. Beltran, C. Munuera, M. Cabero, A. Perez-Munoz, J. Ricote, F. Mompean, M. Garcia-Hernandez, Z. Sefrioui, C. Leon, S. J. Pennycook, M. C. Munoz, M. Varela, J. Santamaria, *Nat. Nanotechnol.* **2017**, *12*, 655.
[17] M. Li, L. L. Tao, J. P. Velev, E. Y. Tsymbal, *Phys. Rev. B* **2018**, *97*, 155121.
[18] D. D. Fong, G. B. Stephenson, S. K. Streiffer, J. A. Eastman, O. Auciello, P. H. Fuoss, C. Thompson, *Science* **2004**, *304*, 1650.
[19] E. Y. Tsymbal, H. Kohlstedt, *Science* **2006**, *313*, 181.
[20] A. Chanthbouala, V. Garcia, R. O. Cherifi, K. Bouzehouane, S. Fusil, X. Moya, S. Xavier, H. Yamada, C. Deranlot, N. D. Mathur, M. Bibes, A. Barthelemy, J. Grollier, *Nat. Mater.* **2012**, *11*, 860.
[21] T. Li, A. Lipatov, H. Lu, H. Lee, J.-W. Lee, E. Torun, L. Wirtz, C.-B. Eom, J. Íñiguez, A. Sinitskii, A. Gruverman, *Nat. Commun.* **2018**, *9*, 3344.
[22] V. Garcia, S. Fusil, K. Bouzehouane, S. Enouz-Vedrenne, N. D. Mathur, A. Barthelemy, M. Bibes, *Nature* **2009**, *460*, 81.
[23] Y. W. Yin, J. D. Burton, Y. M. Kim, A. Y. Borisevich, S. J. Pennycook, S. M. Yang, T. W. Noh, A. Gruverman, X. G. Li, E. Y. Tsymbal, Q. Li, *Nat. Mater.* **2013**, *12*, 397.
[24] J. P. Velev, J. D. Burton, M. Y. Zhuravlev, E. Y. Tsymbal, *npj Comput. Mater.* **2016**, *2*, 16009.
[25] J. Wu, H.-Y. Chen, N. Yang, J. Cao, X. Yan, F. Liu, Q. Sun, X. Ling, J. Guo, H. Wang, *Nat. Electron.* **2020**, *3*, 466.
[26] R. Guo, L. Tao, M. Li, Z. Liu, W. Lin, G. Zhou, X. Chen, L. Liu, X. Yan, H. Tian, E. Y. Tsymbal, J. Chen, *Sci. Adv.* **2021**, *7*, eabf1033.
[27] J. Tornos, F. Gallego, S. Valencia, Y. H. Liu, V. Rouco, V. Lauter, R. Abrudan, C. Luo, H. Ryll, Q. Wang, D. Hernandez-Martin, G. Orfila, M. Cabero, F. Cuellar, D. Arias, F. J. Mompean, M. Garcia-Hernandez, F. Radu, T. R. Charlton, A. Rivera-Calzada, Z. Sefrioui, S. G. E. Te Velthuis, C. Leon, J. Santamaria, *Phys. Rev. Lett.* **2019**, *122*, 037601.
[28] M. Y. Zhuravlev, S. Maekawa, E. Y. Tsymbal, *Phys. Rev. B* **2010**, *81*, 104419.
[29] T. Choi, S. Lee, Y. J. Choi, V. Kiryukhin, S. W. Cheong, *Science* **2009**, *324*, 63.
[30] L. Jiang, W. S. Choi, H. Jeen, S. Dong, Y. Kim, M. G. Han, Y. Zhu, S. V. Kalinin, E. Dagotto, T. Egami, H. N. Lee, *Nano Lett.* **2013**, *13*, 5837.
[31] W. Wu, J. R. Guest, Y. Horibe, S. Park, T. Choi, S. W. Cheong, M. Bode, *Phys. Rev. Lett.* **2010**, *104*, 217601.
[32] R. Du, X. Qiu, A. Li, D. Wu, *Appl. Phys. Lett.* **2014**, *104*, 142907.
[33] S. Lee, B. A. Apgar, L. W. Martin, *Adv. Energy Mater.* **2013**, *3*, 1084.
[34] D. A. Tenne, X. X. Xi, Y. L. Li, L. Q. Chen, *Phys. Rev. B* **2004**, *69*, 174101.
[35] C. B. Eom, R. J. Cava, R. M. Fleming, J. M. Phillips, R. B. Vandover, J. H. Marshall, J. W. Hsu, J. J. Krajewski, W. F. Peck Jr., *Science* **1992**, *258*, 1766.
[36] Y. Du, H. Pan, S. Wang, T. Wu, Y. P. Feng, J. Pan, A. T. Wee, *ACS Nano* **2012**, *6*, 2517.
[37] M. D. Pickett, J. Borghetti, J. J. Yang, G. Medeiros-Ribeiro, R. S. Williams, *Adv. Mater.* **2011**, *23*, 1730.
[38] Y. Hikita, L. F. Kourkoutis, T. Susaki, D. A. Muller, H. Takagi, H. Y. Hwang, *Phys. Rev. B* **2008**, *77*, 670.
[39] E. R. Brown, T. C. L. G. Sollner, C. D. Parker, W. D. Goodhue, C. L. Chen, *Appl. Phys. Lett.* **1989**, *55*, 1777.
[40] P. J. Price, *Phys. Rev. B* **1988**, *38*, 1994.
[41] M. Shikano, T.-K. Huang, Y. Inaguma, M. Itoh, T. Nakamura, *Solid State Commun.* **1994**, *90*, 115.
[42] J. P. Perdew, K. Burke, M. Ernzerhof, *Phys. Rev. Lett.* **1996**, *77*, 3865.
[43] H. T. Jeng, S. H. Lin, C. S. Hsue, *Phys. Rev. Lett.* **2006**, *97*, 067002.
[44] D. Vanderbilt, *Phys. Rev. B* **1990**, *41*, 7892.
[45] P. Giannozzi, S. Baroni, N. Bonini, M. Calandra, R. Car, C. Cavazzoni, D. Ceresoli, G. L. Chiarotti, M. Cococcioni, I. Dabo, A. Dal Corso, S. de Gironcoli, S. Fabris, G. Fratesi, R. Gebauer, U. Gerstmann, C. Gougoussis, A. Kokalj, M. Lazzeri, L. Martin-Samos, N. Marzari, F. Mauri, R. Mazzarello, S. Paolini, A. Pasquarello, L. Paulatto, C. Sbraccia, S. Scandolo, G. Sclauzero, A. P. Seitsonen, et al., *J. Phys.: Condens. Matter* **2009**, *21*, 395502.
[46] M. Y. Zhuravlev, Y. Wang, S. Maekawa, E. Y. Tsymbal, *Appl. Phys. Lett.* **2009**, *95*, 052902.
[47] D. J. Kim, J. Y. Jo, Y. S. Kim, Y. J. Chang, J. S. Lee, J. G. Yoon, T. K. Song, T. W. Noh, *Phys. Rev. Lett.* **2005**, *95*, 237602.
[48] J. H. Barrett, *Phys. Rev.* **1952**, *86*, 118.

© 2022 The Authors. Advanced Materials published by Wiley-VCH GmbH